Low temperature propane oxidation over Co_3O_4 based nano-array catalysts: Ni dopant effect, reaction mechanism and structural stability

Zheng Ren [a], Zili Wu [b,*], Wenqiao Song [c], Wen Xiao [d], Yanbing Guo [a,*], Jun Ding [d], Steven L. Suib [a,c], Pu-Xian Gao [a,*]

[a] Department of Materials Science and Engineering & Institute of Materials Science, University of Connecticut, Storrs, CT 06269-3136, USA
[b] Center for Nanophase Materials Sciences, Oak Ridge National Laboratory, Oak Ridge, TN 37831, USA
[c] Department of Chemistry, University of Connecticut, Storrs, CT 06269, USA
[d] Department of Materials Science and Engineering, National University of Singapore, 119260, Singapore

ARTICLE INFO

ABSTRACT

Low temperature propane oxidation has been achieved by Co_3O_4-based nano-array catalysts featuring low catalytic materials loading (15 mg under flow rate of 150 mL/min). The increased Ni doping into the Co_3O_4 lattice has led to 100% propane conversion at low temperature (<400 °C) and has enhanced reaction kinetics by promoting the surface lattice oxygen activity. *In situ* DRIFTS investigations in tandem with isotopic oxygen exchange reveals that the propane oxidation proceeds *via* a Mars-van Krevelen mechanism where surface lattice oxygen acts as the active site whereas O_2 in the reaction feed does not directly participate in CO_2 formation. The Ni doping promotes the formation of less stable carbonates on the surface to facilitate the CO_2 desorption. The thermal stability of Ni doped Co_3O_4 decreases with increased Ni concentration despite the increased catalytic activity. A balance between enhanced activity and compromised thermal stability is considered in the Ni doped Co_3O_4 nano-array catalysts for hydrocarbon oxidation. This study provides useful and timely guidance for rational catalyst design toward low temperature catalytic oxidation.

© 2015 Elsevier B.V. All rights reserved.

1. Introduction

Hydrocarbon emissions generated from mobile and stationary combustion sources, such as automobiles, petrochemical, and power generation plants, represent a major group of pollutants to the environment [1–3]. With increasingly stringent regulation imposed upon emission control, highly efficient catalysts are in great demand in order to efficiently remove hydrocarbons and other pollutants such as CO, NO_x, and particulate matter. Although Pt group metals (PGM) are still dominant in catalysts for automotive emission control [4–7], considerable attention has been paid to the search for cost-effective and highly efficient new catalysts for catalytic oxidation at low temperature [8–11]. Typical candidates include transition metal oxides [12–15] and complex oxides such as perovskites [16–21]. As a typical transition metal oxide, Co_3O_4 nanostructures have been widely studied to be promising for low temperature catalytic oxidation. For example, mesoporous Co_3O_4 has been reported to achieve complete CO oxidation at −60 °C [22]. Co_3O_4 nanorods with prominent (1 1 0) planes can fully convert CO to CO_2 at −77 °C [23].

Recently, we have successfully invented and demonstrated new catalyst configurations, *i.e.*, the nanostructure-array (nano-array) based monolithic catalysts, where hierarchical nanostructures such as nanowire arrays are integrated onto commercial cordierite honeycombs [24–26]. The unique geometrical and spatial arrangements of nano-array are shown to help reduce catalyst usage by 10–40 times with good catalytic oxidation performance and thermal/mechanical robustness. Furthermore, the porous Co_3O_4 nano-array based monolithic catalysts have demonstrated a remarkable 80% NO to NO_2 conversion at temperatures lower than 300 °C, displaying a much better catalytic oxidation performance than wash-coated Pt monolithic catalysts, *i.e.*, with higher efficiency, lower reaction temperature and cost [27]. We have further showcased the scalable fabrication of transition metal doped Co_3O_4 nano-array catalysts featuring complete methane oxidation activ-

ity at temperatures below 600 °C with catalyst usage lower than 20 mg [28]. Specifically, Ni doping was found to enhance the catalytic activity for the catalyst performance at lower temperatures. By first-principle calculations we found that the incorporation of Ni into the spinel Co_3O_4 lattice facilitated the interaction between hydrocarbons and lattice oxygen [28]. However, more experimental evidence through detailed investigations upon the reaction mechanism is still required to better interpret the Ni doping effect for rational catalyst design toward low temperature hydrocarbon oxidation.

In this study we demonstrated a similar effect of Ni doping that led to enhanced reaction kinetics for low temperature propane oxidation by promoting lattice oxygen activity. *In situ* DRIFTS in tandem with oxygen isotope exchange were employed to reveal a Mars-van Krevelen reaction mechanism where surface lattice oxygen acted as the active sites. The Ni doping effects upon structure stability studied by Raman scattering, XPS, and XRD indicate that a balance between promoted catalytic activity and decreased thermal stability for Ni doped Co_3O_4 nano-arrays is needed for practical applications.

2. Experimental

2.1. Synthesis of Ni-doped Co_3O_4 and pristine Co_3O_4 nanowire arrays

Hierarchical nickel cobaltite nanowire array catalysts were prepared *via* a facile solution chemistry strategy as we previously reported [27,28]. Briefly, the monolithic honeycomb substrate was first immersed in distilled water and acetone and sonicated for 30 min to remove residual contaminants inside the channels. For synthesis of $Ni_xCo_{3-x}O_4$ nanowires, aqueous solutions of cobalt nitrate hexahydrate ($Co(NO_3)_2 \cdot 6H_2O$) and nickel nitrate hexahydrate ($Ni(NO_3)_2 \cdot 6H_2O$) with adjusted concentration ratio were prepared as the precursors for the reaction. The monolithic honeycomb was then suspended in 100 mL of the as-prepared precursor solution followed by the addition of 3 g urea under vigorous magnetic stirring until the solution becomes transparent. The reaction was maintained at 90 °C for 12 h. The honeycomb substrate was then rinsed with distilled water and dried at 80 °C for 4 h. Ambient annealing at 300 °C for 4 h with a ramp rate of 20 °C/min transforms the basic-carbonate nanowires into porous oxide. For synthesis of Co_3O_4 nanowires, two types of cobalt precursors, cobalt nitrate and cobalt chloride, were used with all other reaction conditions unchanged. The as-prepared nanowires were denoted as Co_3O_4 and Co_3O_4–Cl, respectively.

2.2. Catalyst characterization

The structure characterization of nanowires has been performed with electron microscopy. Specifically, the morphology and structure were characterized using a field emission scanning electron microscope (FE-SEM, JEOL 6335F) and a high resolution transmission electron microscope (HRTEM, JEOL JEM-2010, 200 kV). The TEM samples were prepared by scratching nanowires off the honeycombs and dispersing in ethanol, which was then dropped onto the copper grid coated with carbon film. The elemental distribution was investigated by scanning transmission electron microscopy (STEM) based on the energy dispersive X-ray spectrometry (EDS).

The BET surface area was characterized with a Quantachrome NOVA 1000 Gas Sorption Analyzer and Micromeritics ASAP 2020 physisorption analyzer. The temperature-programmed desorption of O_2 (O_2-TPD) as well as the temperature-programmed reduction by H_2 (H_2-TPR) was conducted in a tube furnace equipped with a gas analyzer MKS coupled with a quadrupole mass selective detec-

tor. The temperature was controlled with a WATLOW F4 controller. The catalyst (200 mg) was packed in a quartz tube reactor mounted within the tube furnace. The loaded sample was first purged under 10% O_2 flow at 300 °C for 1 h and then cooled down to room temperature. For O_2-TPD, the sample was exposed to pure oxygen for 1.5 h at room temperature. The catalyst was then purged with argon for 30 min to remove any surface physisorbed gases and residual feed gas from the streams. After purging, the catalyst was heated under a flow of argon from room temperature to 800 °C with a heating ramp of 10 °C/min. For H_2-TPR, the sample was exposed to 1% H_2 balanced with argon. With temperature ramping from room temperature to 800 °C at a rate of 10 °C/min, the H_2 consumption was simultaneously monitored by mass spectrometry. The flow rate for all these steps was controlled to be 200 sccm.

2.3. Catalytic performance test

A BenchCAT reactor (Altamira Instruments) was used for propane oxidation tests. A mass spectrometer and Agilent Micro-GC were equipped for the gas species analyses in the product stream. Catalytic performance tests were carried out in a temperature range of 20–800 °C using 15 sccm of 10% C_3H_8/N_2, 15 sccm of pure O_2, and 120 sccm of argon (1% C_3H_8, 10% O_2, 9% N_2 and 80% Ar) with a total flow rate of 150 sccm. Three pieces of monolithic nano-array honeycomb catalysts (2 × 3 channels in cross section and 1 cm long in channel length for each piece) were loaded into the quartz tube with inner diameter of ¼ inch (~0.64 cm). The space velocity was thus controlled to be ~45,000/h. The total weight of the three pieces of the monolithic nano-array honeycomb was around 0.15 g. Considering the 10–13% nano-array loading, the actual catalytic active materials were about 15–20 mg.

2.4. in situ DRIFTS study of catalyst

To reveal the reaction mechanism during the catalytic reaction, DRIFTS was employed to characterize the chemical species on the catalyst surface. The catalyst (3 mg) was first mixed with 30 mg CaF_2 by grinding to render fine powders for IR characterization. IR spectra were collected using a Thermo Nicolet Nexus 670 spectrometer in diffuse reflectance mode (DRIFT) while the outlet stream was analyzed with a quadrupole mass spectrometer (QMS) (OmniStar GSD-301 O2, Pfeiffer Vacuum). A Pike Technologies HC-900 DRIFTS cell with volume of 6 mL was used as the *in situ* reaction chamber where powdered catalyst was placed.

In C_3H_8 oxidation experiments, 30 mg fine powders (cobaltite nanowires mixed with CaF_2) were loaded into the DRIFT cell and were pretreated in 10% O_2 at 300 °C for 1 h and the temperature was then slowly reduced to room temperature in the same atmosphere. Before the powders were exposed to the reaction gas mixture, they were first purged by helium to remove any adsorbed residuals on the catalyst surface. The reaction gas mixture consists of 1% C_3H_8, 10% O_2 balanced by helium with the total flow rate controlled to be 30 sccm so that the space velocity was kept the same as that in the catalytic performance test. The reaction gas and helium were alternatively switched on to characterize the chemical species on the catalyst surface. Specifically, a series of IR spectra as well as QMS profiles were continuously collected in the reaction gas mixture as the reaction proceeded at each temperature. After about 8 min of exposure to the reaction gases, the catalyst was purged with helium for the next 7 min during which IR spectra were also collected to reveal the surface chemical species. All the reported IR spectra are difference spectra referenced to background spectra collected at each temperature after the pretreatment but prior to C_3H_8 oxidation reaction or C_3H_8–TPR.

In C_3H_8–TPR experiments, a similar protocol was adopted. Fine powders (30 mg cobaltite nanowires mixed with CaF_2) were pre-

treated in 10% O_2 at 300 °C for 1 h and the temperature was then slowly reduced to room temperature in the same atmosphere. Before the powders were exposed to 1% C_3H_8 (total flow rate: 30 sccm), they were purged by helium to remove any adsorbed residuals on the catalyst surface. A series of IR spectra and QMS profiles were collected when the 1% C_3H_8 was introduced. At each temperature, the propane gas was switched off after 3 min and the catalyst was purged by helium with IR spectra and QMS profiles recorded.

2.5. Surface oxygen replacement by isotopic $^{18}O_2$

The catalyst was first purged by 10% O_2 at 300 °C for 1 h which was the pretreatment condition before the catalytic performance tests. Helium was then introduced and the temperature was increased from 300 °C to 450 °C. The catalyst was kept in helium atmosphere at 450 °C for 15 min before 2% $^{18}O_2$ (ISOTEC, Sigma–Aldrich) was introduced (flow rate 30 sccm, balanced by helium) to initiate the surface lattice oxygen exchange. After another 15 min, the temperature was reduced to room temperature in the same atmosphere (2% $^{18}O_2$) and the catalyst was again purged by helium before the IR spectra for the propane oxidation in $^{16}O_2$ were collected.
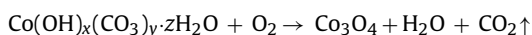
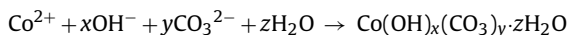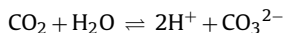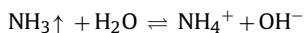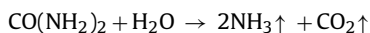### 2.6. Raman spectroscopy and X-ray photoelectron spectroscopy

Raman scattering spectra were recorded by a triple Raman spectrometer (Princeton Instrument Acton Trivista 555) equipped with a customized ellipsoidal mirror and a fiber optics bundle. Edge filters were used in front of the fiber optics bundle to block the laser irradiation ($\lambda_{ex.}$ = 532 nm) and a UV-enhanced liquid nitrogen cooled CCD detector was responsible for the signal detection and monitoring. Cyclohexane was employed as a standard for all the Raman shift calibrations. X-ray photoelectron spectroscopy (XPS) was performed with a Kratos Analytical (Axis Ultra DLD) instrument equipped with monochromatic Al Kα source operating at 1486.7 eV. The signal was filtered with a hemispherical analyzer (pass energy 160 eV for survey spectra and 20 eV for narrow high resolution scans). The C 1s photoelectron line at 284.6 eV was used as an internal standard for correction of charging effects in all samples.

3. Results

3.1. Structure characterization of nano-array catalysts by electron microscopy

The SEM images in Fig. 1a through Fig. 1c display the morphology and orientation of hierarchical Ni doped and pristine Co_3O_4 nanowires on the monolithic cordierite honeycombs. The morphology characteristics are consistent with our previous reports [24,27,28]. Briefly, nanowires have smaller diameters when nitrate is used as the precursor in the synthesis. As illustrated in Fig. 1c, cobalt chloride leads to nanowires with sharp tips and the nanowires are arranged into arrays in a more orderly way while cobalt nitrate gives rise to compact alignment of hierarchical nanoflowers. Meanwhile, no phase segregation is observed when Ni is added as dopant and the hierarchical nano-arrays retain their morphology. The corresponding HRTEM images in Fig. 1d through Fig. 1f reveal the crystalline nature of all the nanowires. The nanowires are shown to be porous by regular TEM imaging. Fig. 2a shows that each individual nanowire is composed of multiple interconnected crystallites and voids can be easily seen within nanowires. Elemental mapping under STEM mode clearly reveals the homogeneous distribution of Ni in the nanowires which further

confirms the successful doping of Ni in the Co_3O_4 lattice. A considerable amount of Cl has been detected by EDS in Co_3O_4–Cl nanowires. The existence of surface Cl can be ascribed to the formation of different precursors from the urea hydrolysis in the synthesis. Previous studies show that the preparation of Co_3O_4 nanowires involves several chemical reactions [29–31].

$$CO(NH_2)_2 + H_2O \rightarrow 2NH_3\uparrow + CO_2\uparrow$$

$$NH_3\uparrow + H_2O \rightleftharpoons NH_4^+ + OH^-$$

$$CO_2 + H_2O \rightleftharpoons 2H^+ + CO_3^{2-}$$

$$Co^{2+} + xOH^- + yCO_3^{2-} + zH_2O \rightarrow Co(OH)_x(CO_3)_y \cdot zH_2O$$

$$Co(OH)_x(CO_3)_y \cdot zH_2O + O_2 \rightarrow Co_3O_4 + H_2O + CO_2\uparrow$$

However, when chloride is used as precursor the chloride ion participates in the reaction which results in the formation of $Co(OH)_x(CO_3)_y Cl_k \cdot zH_2O$ that further decomposes into Co_3O_4 with chlorine on the surface. The effect of chlorine upon the catalyst performance will be discussed later.

3.2. Propane oxidation performance and reaction kinetics

Fig. 3a exhibits the light-off curves of catalytic propane oxidation by three different nano-arrays. The Ni doped Co_3O_4 nano-arrays ($Ni_{0.27}Co_{2.73}O_4$) demonstrate the best performance catalyzing propane oxidation at the lowest temperature (full conversion of C_3H_8 into CO_2 at 425 °C) while Co_3O_4–Cl achieves 100% conversion at 500 °C. Compared with pristine Co_3O_4 nano-arrays, Ni doping is observed to enhance the catalytic activity. For example, the temperatures for 20% and 50% conversion of C_3H_8 into CO_2 are 270 °C and 320 °C for $Ni_{0.27}Co_{2.73}O_4$ but are 295 °C and 350 °C for Co_3O_4, respectively. BET surface area analyses were performed by using 0.15 g monolithic nano-array catalysts (nanowires plus honeycomb) where the mass of nanowires were measured by the weight differences before and after the synthesis. The BET surface area of bare cordierite honeycomb was measured to be 0.35 m^2/g. We assume the measured BET surface area of honeycombs structured with nano-arrays from Fig. 3b is approximately the linear summation of contributions from bare cordierite and the grown nano-arrays. The BET surface area of nano-array A_{nw} is thus calculated by

$$A_{nw} = \frac{A(m_{sub} + m_{nw}) - A_{sub}m_{sub}}{m_{nw}}$$

m_{sub}: the mass of cordierite substrate;
m_{nw}: the mass of the nanowire arrays (weight difference of honeycomb substrate before and after nanowires growth);
A_{sub}: the measured BET surface area of bare cordierite substrate;
A: the measured BET surface area of cordierite structured with nano-arrays.

With the different mass loadings and the calculated BET surface areas of nano-arrays summarized in Table 1, the reaction rate for $C_3H_3 + 5O_2 \rightarrow 3CO_2 + 4H_2O$ at certain temperature can be calculated by

$$r = \frac{1\% \times conversion[\%] \times flowrate[L/s]}{22.4 L/mol \times m_{nw}[g] \times A_{nw}[m^2/g]} \left[mol/\left(m^2 s \right) \right]$$

where A_{nw} is the BET surface area of the nanowires. As shown in Fig. 3c, Ni doped Co_3O_4 nano-arrays exhibit higher reaction rates than both Co_3O_4 and Co_3O_4–Cl nano-arrays which confirms the enhanced reaction kinetics and activity after Ni doping. The rate difference between Co_3O_4 and Co_3O_4–Cl nano-arrays is not as obvious
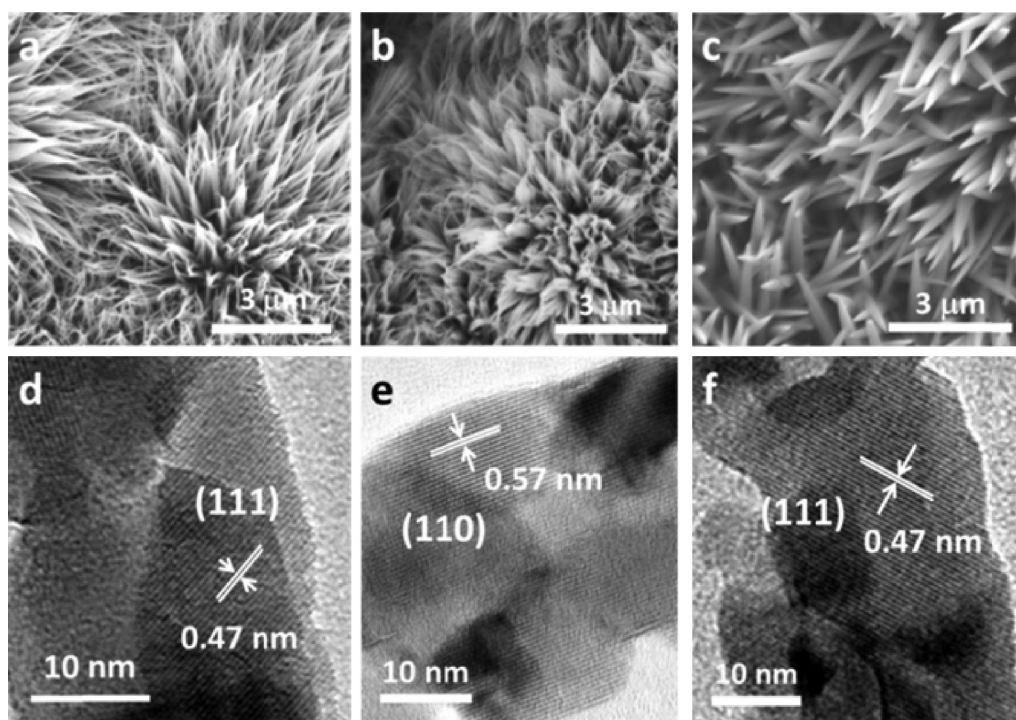
Fig. 1. SEM images of the as-prepared nanowire array catalysts: (a) Co_3O_4 nano-arrays; (b) Ni doped Co_3O_4 nano-arrays ($Ni_{0.27}Co_{2.73}O_4$); (c) Co_3O_4 nano-arrays prepared by chloride. High resolution TEM characterization of (d) Co_3O_4 nanowires; (e) $Ni_{0.27}Co_{2.73}O_4$ nanowires and (f) Co_3O_4 nanowires (Co_3O_4–Cl) prepared by chloride.

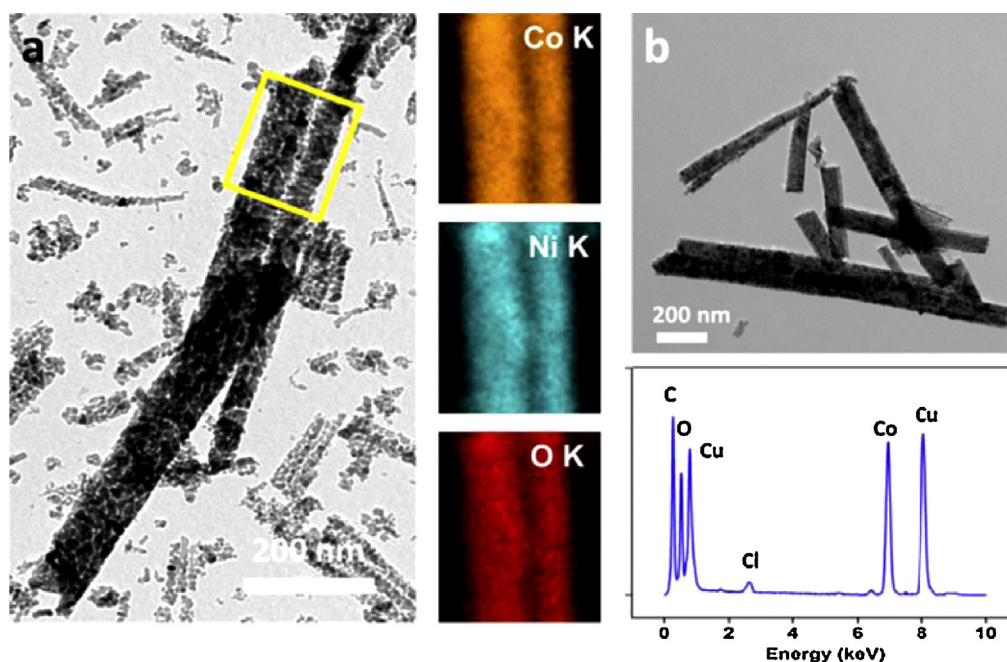**Fig. 2.** (a) TEM image of $Ni_{0.27}Co_{2.73}O_4$ nanowires and the associated STEM mapping of the selected region showing the uniform distribution of Ni, Co and O within the nanowires; (b) TEM characterization of Co_3O_4–Cl nanowires and the EDS spectrum.

Table 1
Summary of structure and reaction characteristics for nano-array catalysts.

Sample	Mass loading (mg)	Surface area (m²/g)	T_{50} (°C)	T_{100} (°C)	Ea (kJ/mol)
$Ni_{0.27}Co_{2.73}O_4$	13	148.3	320	425	32.5
Co_3O_4	13.6	151.1	350	450	62.5
Co_3O_4–Cl	16.7	81.1	385	500	83.8

T_{50}: The temperature at which 50% conversion of C3H8 is achieved; T_{100}: the temperature at which 100% conversion of C3H8 is achieved; Ea: the calculated apparent activation energy (when conversion <10%).
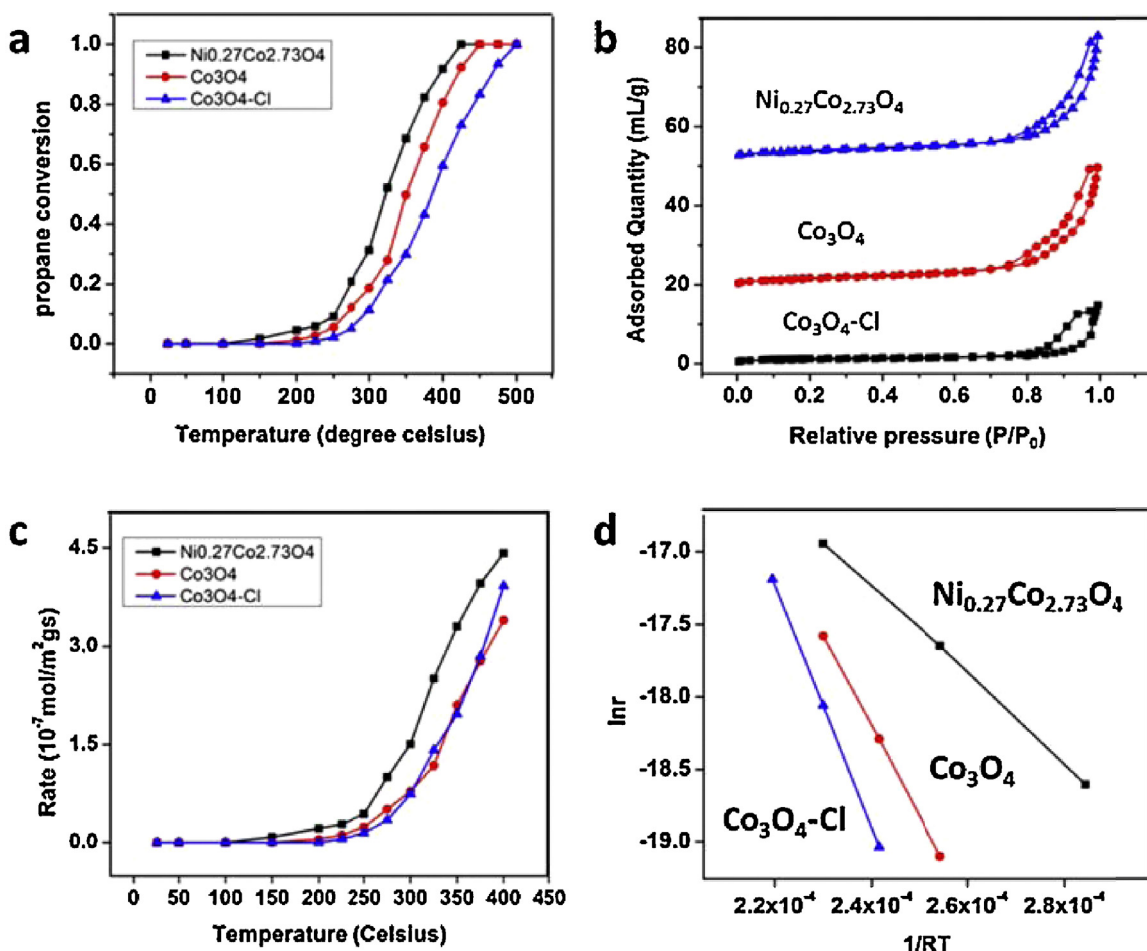
Fig. 3. (a) Light-off curves for catalytic propane oxidation by nano-arrays catalysts; (b) BET surface area characterization of nano-arrays catalysts; (c) Comparison of reaction rates of different nano-arrays; (d) Arrhenius plots and apparent activation energy calculations for different nano-arrays.

as those displayed in Fig. 3a. The rate of Co_3O_4 nano-arrays converting C_3H_8 to CO_2 is only slightly higher than that of Co_3O_4–Cl nano-arrays in the low temperature region (<300 °C) while at high temperature the rates are almost identical. The inferior reaction activity of Co_3O_4–Cl nano-array revealed by conversion light-off in Fig. 3a may result from its smaller surface area. To better reveal the reaction kinetics, the apparent activation energies are calculated when C_3H_8 conversion is lower than 10%. For propane oxidation, the reaction rate can be expressed as $r = k\,[C_3H_8]^a\,[O_2]^b$ because the reaction is irreversible in the O_2 rich atmosphere ($C_3H_8/O_2 = 1/10$). Using the Arrhenius equation, $r = A\exp\left(-\frac{E_a}{RT}\right)[C_3H_8]^a[O_2]^b$ where E_a represents the apparent activation energy. When the propane conversion is very low (<10%), the concentrations of both C_3H_8 and O_2 are approximately constant and the correlation between ln r and 1/RT is thus close to linear.

$$\ln r = -\frac{E_a}{RT} + \ln A + a\ln[C_3H_8] + b\ln[O_2]$$

Ni doped Co_3O_4 nano-arrays exhibit enhanced reaction kinetics with the lowest apparent activation energy (E_a = 32.5 kJ/mol) and the Co_3O_4–Cl nano-array is kinetically sluggish (E_a = 83.8 kJ/mol). The reaction kinetics study confirms the Ni doping is able to promote catalyst activity and surface chlorine hinders the catalytic conversion at low temperature.

3.3. Redox property and lattice oxygen activity

Redox properties of nano-arrays catalysts have been investigated by H_2-TPR with H_2 consumption monitored by online QMS. Two reduction peaks were observed in Co_3O_4 based nano-arrays where the one located in the low temperature region around 300 °C corresponds to Co^{3+} reduction to Co^{2+} and the other at 400 °C represents Co^{2+} conversion to metallic Co [22,32]. The incorporation of Ni into the spinel Co_3O_4 lattice leads to better redox properties since the temperatures for both Co^{3+} reduction to Co^{2+} and Co^{2+} to Co^0 are shifted to lower temperature. Similar tendency has been observed in C_3H_8–TPR experiments for $Ni_{0.27}Co_{2.73}O_4$ and Co_3O_4 (Fig. S1). The Co_3O_4–Cl nano-array, however, demonstrates much smaller reduction peaks compared with the other two samples. The smaller reduction peaks suggest that surface chlorine may deactivate Co—O bonds suppressing lattice oxygen interactions with H_2 or C_3H_8. In Fig. 4b, both $Ni_{0.27}Co_{2.73}O_4$ and Co_3O_4 exhibit O_2 desorption at temperature 400-450 °C corresponding to the surface lattice oxygen desorption. The desorption temperature for $Ni_{0.27}Co_{2.73}O_4$ nano-array is 40 °C lower than that of Co_3O_4 indicating surface lattice oxygen is more active. However, almost no desorption has been observed at the same temperature region for Co_3O_4–Cl which further implies Co—O bonding could be passivated by surface chlorine.

3.4. in situ DRIFTS study for propane oxidation

In situ DRIFTS was employed during propane oxidation to reveal more details of the reactions on catalyst surfaces and to identify
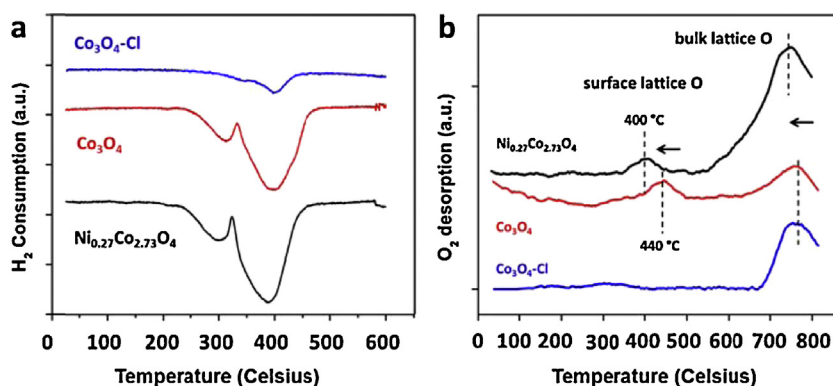
Fig. 4. (a) Redox property investigation upon nano-arrays by H_2–TPR; (b) lattice oxygen activity study by O_2–TPD.
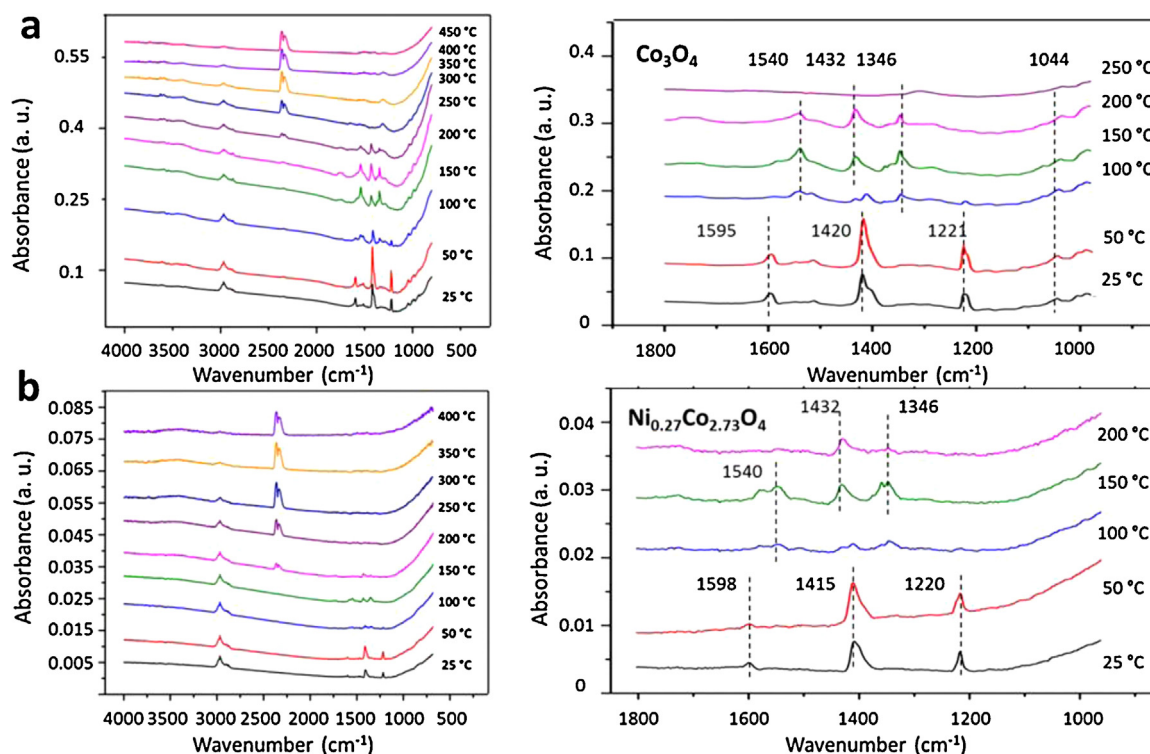

Fig. 5. *In situ* DRIFT spectra for catalytic propane oxidation reactions by (a) Co_3O_4 and (b) $Ni_{0.27}Co_{2.73}O_4$ nano-arrays and the associated DRIFT spectra for surface carbonate identification.

the evolved surface chemical species. In Fig. 5, each spectrum was collected after 8 min reaction at the specified temperature. The bands between 1000 and 1600 cm^{-1} are assigned to various carbonate species. Hydrocarbon and gaseous CO_2 peaks are located around 3000 cm^{-1} and 2350 cm^{-1}, respectively. From DRIFTS spectra massive gaseous CO_2 (wavenumber: 2350 cm^{-1}) production starts at 250 °C for Co_3O_4 and 200 °C for $Ni_{0.27}Co_{2.73}O_4$. These data correspond very well with the light-off curves in Fig. 3. At temperatures higher than 400 °C, negligible amounts of C_3H_8 can be detected indicating full conversion of C_3H_8 to CO_2. At each temperature the gas stream was switched to helium after 8 min reaction and a series of DRIFT spectra were collected to analyze the carbonate species. The right column of Fig. 5 shows the DRIFT spectra after 7 min purging with helium which removes gaseous hydrocarbon species (~3000 cm^{-1}) and CO_2 (2350 cm^{-1}) on the surface. Bicarbonate (1400 cm^{-1}, 1220 cm^{-1}), bidentate carbonate (1595 cm^{-1}, 1044 cm^{-1}) and some uncoordinated CO_3^{2-} (1420 cm^{-1}) are identified at reaction temperatures below 100 °C

Table 2
Assignments of IR bands to related carbonate species on catalyst surface.

Species	IR bands (cm^{-1})
Bicarbonate	1400, 1220
Bidentate carbonate	1595, 1044
Unidentate carbonate	1540, 1044
Polydentate carbonate	1432, 1346
Uncoordinated CO_3^{2-}	1420

for both nano-arrays [33,34]. As the reaction temperature increases above 150 °C, unidentate (1540 cm^{-1}, 1044 cm^{-1}) and polydentate carbonates (1432 cm^{-1}, 1346 cm^{-1}) become the major surface species [34–36]. It seems Ni doping does not affect the nature of surface carbonate species. The assignment of IR bands to carbonate species is summarized in Table 2. For Co_3O_4–Cl the collected *in situ* DRIFT spectra are shown in Fig. S2. Compared with Co_3O_4 nano-array, very small amounts of carbonates have been produced on the Co_3O_4–Cl surface. This indicates that surface chlorine may either
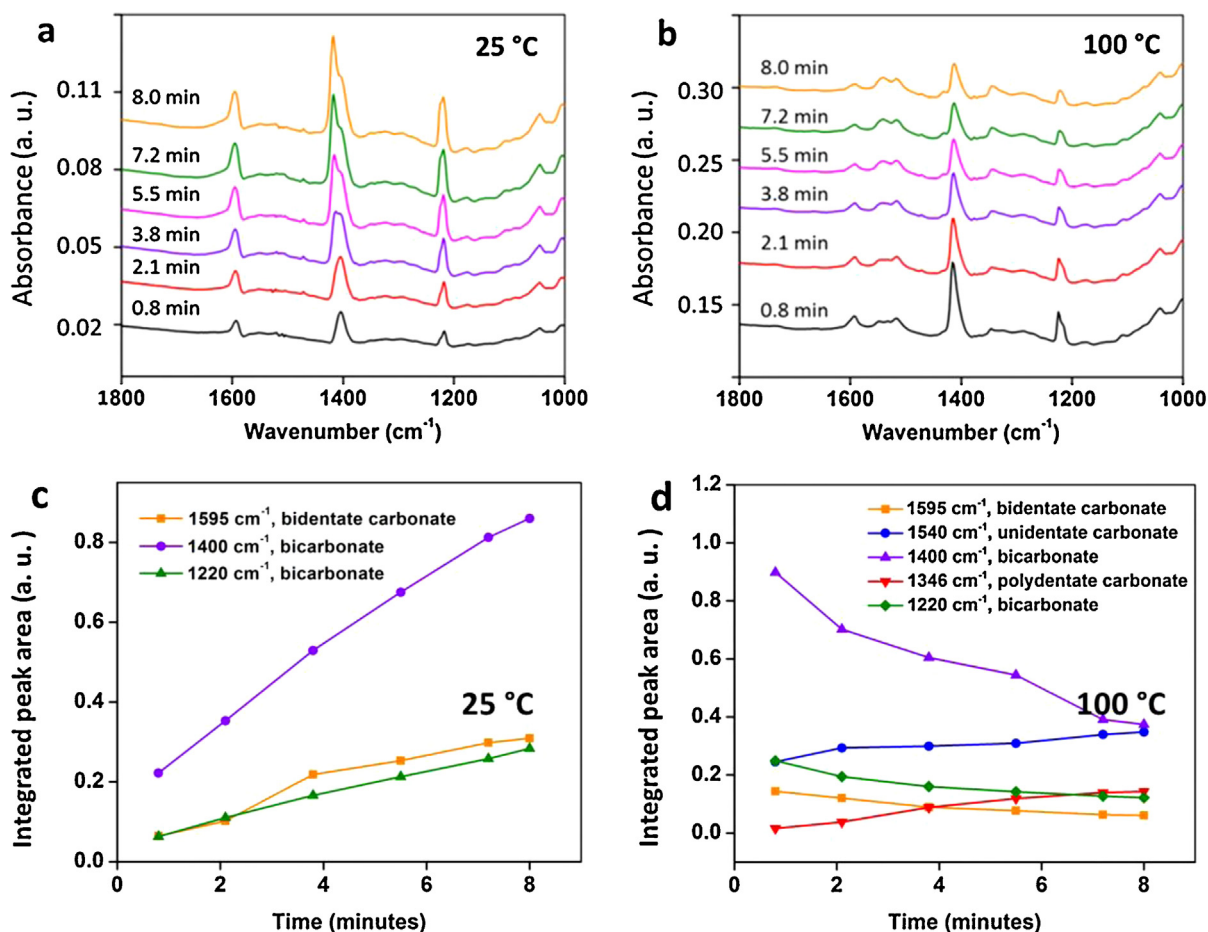
Fig. 6. (a and b) Time dependent in situ DRIFT spectra for propane oxidation at 25 °C and 100 °C revealing the dynamic evolution of surface carbonates on Co_3O_4 nano-arrays; (c and d) Calculated peak areas indicating the dynamic quantity change of typical carbonates.

block the active sites or passivate the lattice oxygen which leads to the sluggish reaction kinetics of Co_3O_4–Cl nano-arrays toward propane oxidation at low temperature.

Two important features are worth noticing in Fig. 5 (1) 100 °C is a critical temperature at which the carbonate species start to transform from bicarbonate and bidentate carbonate to unidentate and polydentate carbonates; (2) at 250 °C the formed carbonates seem thermally unstable since the IR spectrum collected after helium purging differs from the one collected after 8 min reaction. It is thus necessary to study the dynamic evolution of carbonate species at different temperatures. Fig. 6 shows the in situ DRIFT spectra collected during propane oxidation at 25 °C and 100 °C with the dynamic carbonate quantity change revealed by integrating the corresponding peak areas. Carbonates rapidly appear on the catalyst surface even when the reaction time is less than 1 min. At 25 °C the bicarbonate and bidentate carbonate concentrations will not be saturated even for reactions lasting for more than 8 min. However, the intensity of bicarbonate and bidentate carbonate peaks gradually declines at 100 °C while the peaks of unidentate ($1540 \, cm^{-1}$) and polydentate carbonates ($1346 \, cm^{-1}$) start to be obvious. This coincides with Fig. 5 that a mixture of different carbonates exists at 100 °C and with temperature further increased to 150 °C bicarbonate and bidentate carbonate will disappear. However, both unidentate and polydentate carbonates are not stable above 200 °C. Fig. S3 depicts the evolution of carbonates formed during propane oxidation at 250 °C after helium is purged. The intensity of peaks at $1432 \, cm^{-1}$ and $1346 \, cm^{-1}$ (polydentate carbonate) as well as $1540 \, cm^{-1}$ (unidentate) drastically decay after

one minute. The decomposition temperatures of unidentate and polydentate carbonates should be above 250 °C. Meanwhile, bicarbonate and bidentate carbonate are only stable below 150 °C as confirmed by both temperature dependent DRIFT in Fig. 5 and time dependent DRIFT spectra in Fig. 6.

3.5. In situ DRIFTS study for C_3H_8–TPR

In addition to in situ DRIFTS studies of propane oxidation, a series of DRIFT spectra were also recorded for the C_3H_8–TPR process. Fig. 7 displays the DRIFT spectra collected at the Co_3O_4 and $Ni_{0.27}Co_{2.73}O_4$ catalysts surface after introducing 1% C_3H_8 for 3 min followed by helium purging. Similar carbonates are produced at temperatures lower than 200 °C in the absence and presence of gaseous O_2. Bicarbonate, bidentate carbonate, and some uncoordinated CO_3^{2-} still appear at low temperature (<100 °C) while unidentate and polydentate carbonate are formed above 150 °C. Compared with the DRIFT spectra of propane oxidation in Fig. 5, the IR band intensities are weak in the TPR process due to the shorter exposure to propane (3 min). Since the surface carbonate formation is independent on the O_2 in the reaction feed, carbonates are speculated to be produced from propane interactions with surface lattice oxygen. The propane oxidation follows the Mars-van Krevelen mechanism where surface lattice oxygen acts as the reaction active sites [23,37–39]. This proposed reaction mechanism will be further studied later by isotope experiments.
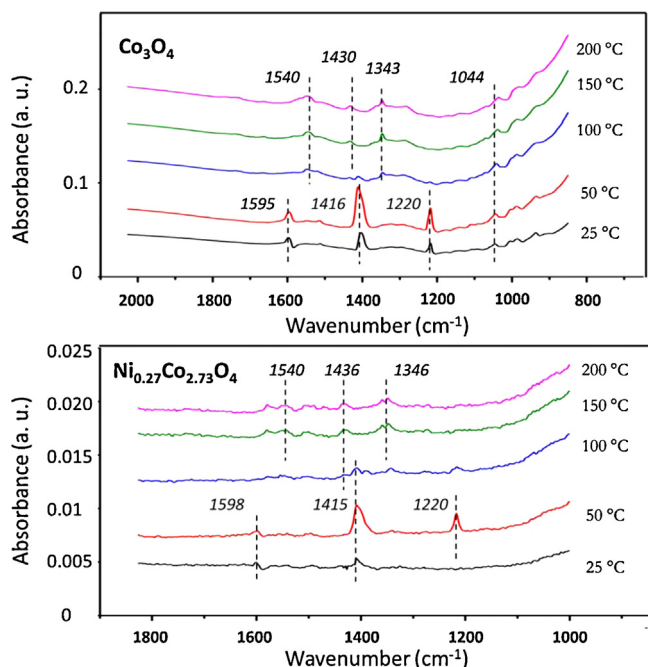
Fig. 7. *In situ* DRIFT spectra recorded for surface carbonate identification during C_3H_8–TPR of Co_3O_4 and Ni-doped Co_3O_4 nano-arrays.

4. Discussion

4.1. Enhanced reaction kinetics by Ni doping

As illustrated in Fig. 3 the Ni doping of Co_3O_4 leads to enhanced catalytic propane oxidation performance. The temperature programmed H_2 and C_3H_8 reductions both reveal the better redox properties of $Ni_{0.27}Co_{2.73}O_4$ nano-arrays by enabling reaction with H_2 and C_3H_8 at lower temperature. Temperature programmed O_2 desorption analysis confirms that surface lattice oxygen can be activated by introducing Ni into the spinel lattice. The enhanced lattice oxygen activity results from the enriched surface oxygen defects in Ni-doped Co_3O_4 as verified in our previous study [28]. When Ni is incorporated to the Co_3O_4 lattice, Co atoms are replaced in the octahedral site where Co has six coordination O atoms. The octahedral Co exhibits a valence state Co^{3+} while the substitute Ni has a valence state of Ni^{2+}. Such loss of positive charges is compensated by creating oxygen vacancies to retain the charge neutrality. The existing oxygen defects result in unsaturated surface lattice oxygen which is more active. Since the *in situ* propane oxidation and propane-TPR investigation by DRIFTS show that catalytic propane oxidation proceeds *via* a Mars-van Krevelen mechanism, the surface lattice oxygen activity is responsible for the reaction kinetics at low temperature. The Ni doping enhances the surface lattice oxygen activity by creating rich oxygen defects on the catalyst surface and therefore promotes the reaction kinetics.

In addition, the DRIFTS study has shown that formation of carbonates is an important step for the catalytic propane oxidation at low temperature. However, the different reaction kinetics should not result from different surface reactions because both Ni doped Co_3O_4 and pristine Co_3O_4 nano-arrays produce the same types of carbonate species. Temperature programmed CO_2 desorption was employed to study the quantity of carbonates produced on catalyst surfaces at different temperatures. Reaction feed (1% C_3H_8, 10% O_2 balanced by helium, flow rate 30 sccm) was introduced to the catalyst surface (30 mg catalyst powder) and the reaction was sustained for 15 min at 25 °C and 150 °C, respectively. Helium was then switched on for purging and the temperature was slowly

reduced to 25 °C. CO_2 desorption was monitored by QMS when the temperature was ramped from 25 °C to 600 °C. In Fig. 8a, the carbonates formed by reaction at 25 °C have a desorption peak at 144 °C and those formed at reaction temperature of 150 °C desorb at 220 °C. This observation is consistent with some features revealed by the DRIFT spectra in Fig. 5. At 25 °C, bicarbonate and bidentate carbonate are the major surface carbonate species which begin to disappear when the temperature is elevated to 150 °C. Both bicarbonate and bidentate carbonate are not stable above 150 °C. Therefore 144 °C seems to be the critical temperature for decomposition. Moreover, this also verifies the coexistence of bicarbonate, bidentate, unidentate, and polydentate carbonate at 100 °C while only unidentate and polydentate are detected at 150 °C. From CO_2-TPD, unidentate and polydentate carbonate decompose at 220 °C which coincides with the fact that no carbonate can be detected in DRIFTS during reaction at temperatures above 250 °C.

More carbonates are formed on the surface of $Ni_{0.27}Co_{2.73}O_4$ nano-array at reaction temperature of 25 °C (integrated QMS peak area: $Ni_{0.27}Co_{2.73}O_4$ 2.21×10^{-8} > Co_3O_4 1.94×10^{-8}) while at 150 °C there is a larger quantity of carbonates on the Co_3O_4 surface (integrated QMS peak area: $Ni_{0.27}Co_{2.73}O_4$ 2.63×10^{-8} < Co_3O_4 3.59×10^{-8}). This may suggest that Ni doping favors the formation of bicarbonate and bidentate carbonate. As more carbonate was generated within the same reaction time, the interaction between propane and lattice oxygen was promoted on Ni doped Co_3O_4 surfaces. However, the CO_2 formation rate is not only dependent on how fast propane interacts with lattice oxygen to form carbonate but also is dependent on how easily the carbonates will decompose. Given bicarbonate and bidentate carbonate are less thermally stable than unidentate and polydentate carbonate [40], the Ni doping is able to facilitate CO_2 formation from carbonate decomposition which leads to enhanced reaction kinetics at low temperature (<150 °C). The larger quantity of carbonates produced on Co_3O_4 surfaces at higher temperature may be ascribed to the larger surface lattice oxygen concentration of Co_3O_4 as revealed by XPS (Fig. 11). Since these carbonates are more stable and are thus more difficult to desorb, they might hinder the further interaction between propane and surface oxygen. The effect of Ni doping upon the catalytic performance has been further demonstrated in Fig. 8b where the light-off curves for $Ni_xCo_{3-x}O_4$ nano-arrays are exhibited. The increased Ni concentration has led to propane conversion at lower temperature.

4.2. Reaction mechanism verification

To further validate the previously proposed Mars-van Krevelen reaction mechanism, *in situ* DRIFTS study has been employed during the propane oxidation on the isotopic $^{18}O_2$ treated catalyst surface (Fig. S4) where surface lattice oxygen ^{16}O has been replaced by ^{18}O at 450 °C. Fig. 9 shows the comparison of the DRIFT spectra collected at the different catalyst surfaces (pretreated with $^{16}O_2$ and $^{18}O_2$) during propane oxidation ($^{16}O_2$ in reaction feed) from 25 °C to 200 °C. As can be seen in Fig. 9a, bicarbonate and bidentate carbonate still appear at low temperature on the $^{18}O_2$ treated surface. However, the bands shift to lower wave numbers because of isotopic ^{18}O in the carbonate. For example, the bicarbonate peak shifts from original 1222 cm^{-1} to 1215 cm^{-1} and bidentate carbonate shifts from 1595 cm^{-1} to 1586 cm^{-1}. Propane clearly still interacts with surface oxygen (^{18}O) even in the presence of $^{16}O_2$ in the reaction feed. As reaction temperature is increased to 100 °C, unidentate and polydentate carbonates start to form with the bands shifted to lower wavenumbers, *e.g.*, 1540 cm^{-1} shifts to 1530 cm^{-1}. However, as the reaction proceeds no such shift can be observed at higher temperature (150 °C and 200 °C) and the previously shifted band goes back to its original position (1530 cm^{-1} back to 1540 cm^{-1}) making the DRIFT spectra identical to those
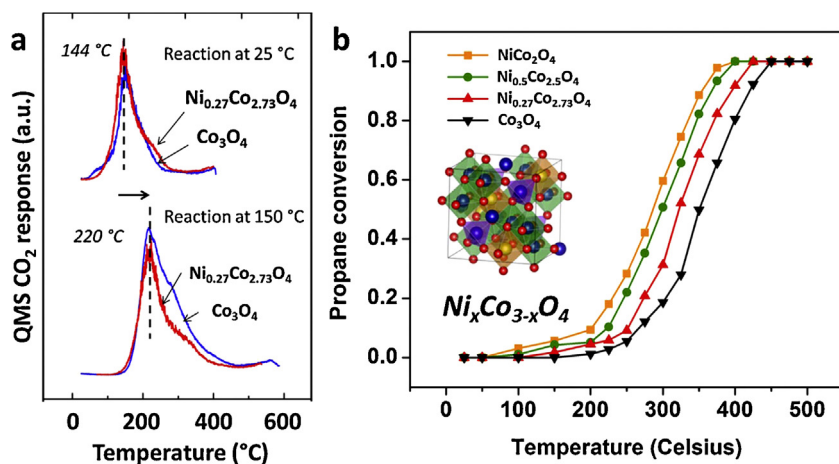
Fig. 8. (a) The measured quantity of surface carbonates generated at low and high reaction temperatures on Ni-doped Co_3O_4 and Co_3O_4 nano-arrays by temperature-programmed CO_2 desorption (CO_2–TPD); (b) catalytic propane oxidation performance of $Ni_xCo_{3−x}O_4$ nano-arrays with controlled Ni concentrations.
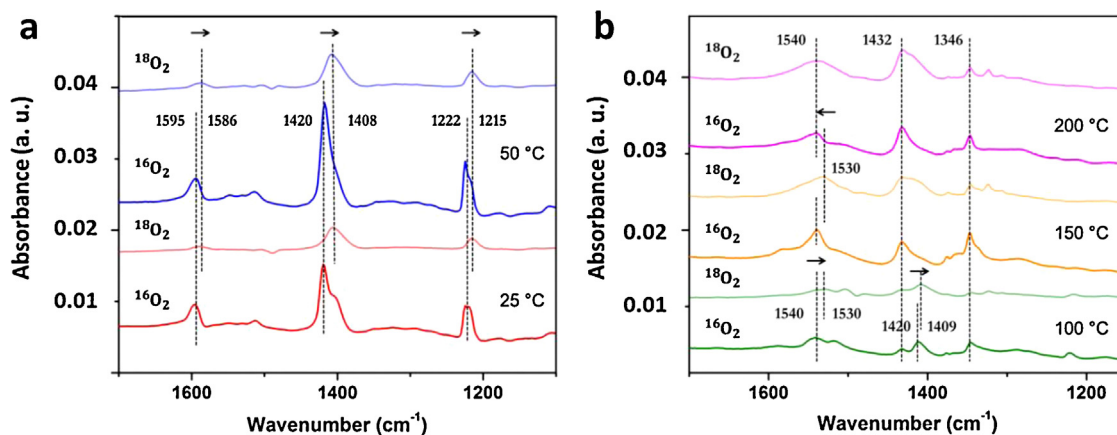

Fig. 9. *In situ* DRIFT spectra recorded for comparison of surface carbonates formed during propane oxidation (in $^{16}O_2$ atmosphere) on $^{16}O_2$ and $^{18}O_2$ treated $Ni_{0.27}Co_{2.73}O_4$ nanowire surfaces.
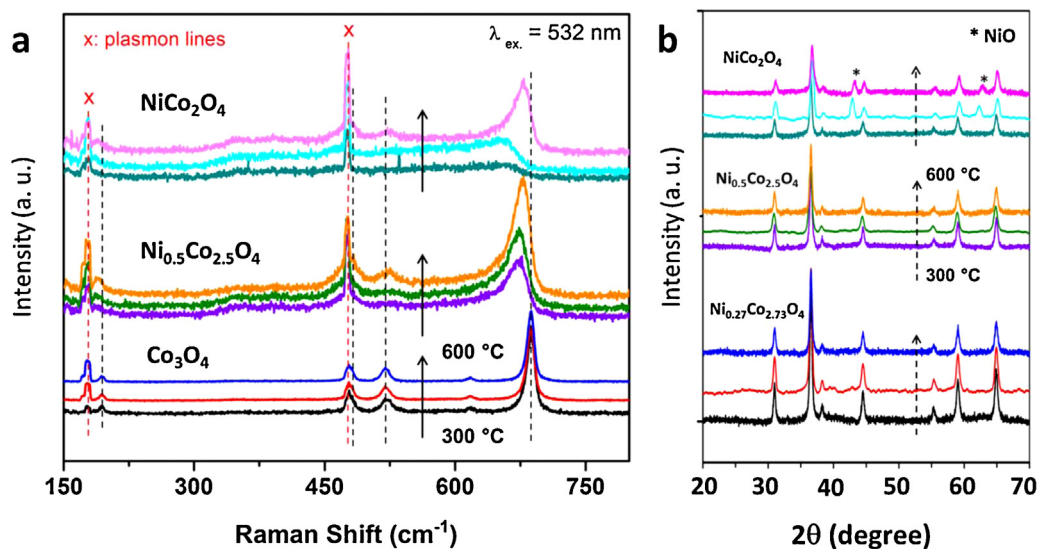

Fig. 10. (a) Raman scattering spectra for $Ni_xCo_{3−x}O_4$ nano-arrays of adjusted Ni concentrations that are annealed at different temperatures (300 °C, 450 °C and 600 °C); (b) XRD patterns for Ni doped Co_3O_4 nano-arrays at different temperatures.
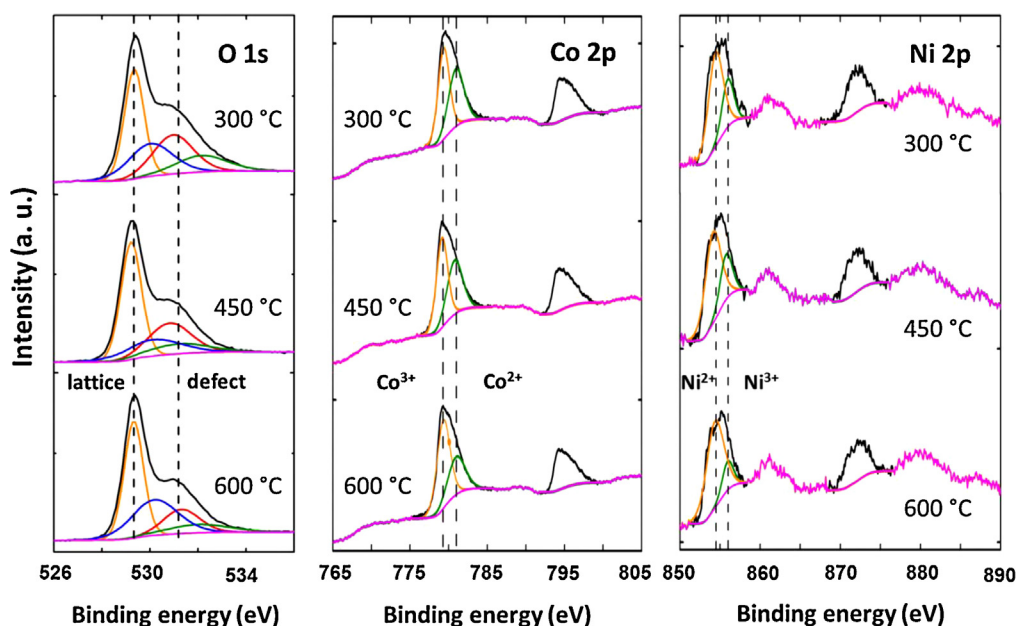
Fig. 11. X-ray photoelectron spectra of $Ni_xCo_{3-x}O_4$ (x = 0.5) nano-arrays after ambient annealing at different temperatures, revealing the tunable oxygen defect population and surface chemical valence states.

pretreated with $^{16}O_2$. Surface ^{18}O has been gradually consumed and the surface lattice oxygen has been replenished by the gas phase $^{16}O_2$. Therefore the carbonates formed at extended reaction times and at higher temperature do not contain ^{18}O and the band shift will no longer be observed. Based on this DRIFTS observation together with the previous results, the catalytic propane oxidation on Co_3O_4-based nano-arrays proceeds *via* the Mars-van Krevelen mechanism where propane interacts with surface lattice oxygen and the oxygen vacancies created by CO_2 desorption are replenished by gaseous O_2. The O_2 in the reaction feed does not directly contribute to CO_2 formation.

4.3. Ni doping effect on catalyst stability

Both this study and our previous results have demonstrated the Ni doping enhances reaction kinetics and promotes hydrocarbon oxidation at low temperature [28]. However, $Ni_xCo_{3-x}O_4$ has been reported to not be stable at high temperature (>400 °C) especially when the Ni concentration is high [41,42]. Raman scattering was applied to study the structural change of Ni doped Co_3O_4 at different temperatures. As shown in Fig. 10a, the black dashed lines mark the characteristic peaks of Co_3O_4 [43]. When the temperature changes from 300 °C to 600 °C, no structural change is observed in Co_3O_4 and thus Co_3O_4 is stable under 600 °C. The incorporation of Ni leads to the shift of characteristic peaks toward lower wavenumbers with suppressed intensity. When the Ni concentration is relatively low ($Ni_{0.5}Co_{2.5}O_4$), the Raman spectra at 300 °C and 450 °C are identical. However, with temperature is elevated to 600 °C, the intensity of Co_3O_4 characteristic peaks starts to increase a little bit indicating the precipitation of Ni out of the spinel lattice. In the case of $NiCo_2O_4$, the increased Ni concentration further deteriorates the structure stability at high temperature. Ni starts to be removed from the lattice at 450 °C corresponding very well with the previous report that the decomposition of $NiCo_2O_4$ takes place above 400 °C. Fig. 10b displays the XRD patterns of Ni doped Co_3O_4 annealed at different temperatures. In the case of $NiCo_2O_4$, NiO precipitates out of the lattice at 450 °C and 600 °C which is consistent with the Raman spectra. $Ni_{0.27}Co_{2.73}O_4$ seems stable below 600 °C with no phase segregation observed in XRD patterns. For $Ni_{0.5}Co_{2.5}O_4$, however, NiO has not been detected by XRD at 600 °C

Table 3
Quantitative results of deconvoluted XPS spectra of O 1s, Co 2p and Ni 2p on the surface population ratios of lattice and defective oxygen, Co^{2+} and Co^{3+}, Ni^{2+} and Ni^{3+}. $2p_{3/2}$ signals were used for the quantitation of Co and Ni valence states.

Annealing temperatures	O 1s O_{latt}/O_{def}	Co 2p Co^{3+}/Co^{2+}	Ni 2p Ni^{2+}/Ni^{3+}
300 °C	1.39	1.17	2.52
450 °C	1.8	1.22	2.66
600 °C	2.56	1.76	4.77

while Raman scattering shows a possible phase transition. Given the small intensity change in Raman spectra, phase segregation may still exist with only a small amount of precipitated NiO.

To better understand the effect of thermal annealing upon $Ni_{0.5}Co_{2.5}O_4$, XPS was utilized to characterize the valence state changes and surface defects. Fig. 11 shows the deconvoluted XPS spectra for O, Co, and Ni in $Ni_{0.5}Co_{2.5}O_4$ after annealing at different temperatures. The broad O 1s peaks can be deconvoluted into four major components (lattice oxygen, surface OH group, oxygen defects, and adsorbed moisture) [44]. The quantitative results in Table 3 reveal high temperature annealing mitigates the oxygen defects (vacancies) on the surface. Despite only small differences in the ratios of lattice O/defective O, Co^{3+}/Co^{2+} and Ni^{2+}/Ni^{3+} are observed at 300 °C and 450 °C, annealing at 600 °C results in a drastic population increase of Ni^{2+} and lattice oxygen. The increase of Co^{3+} concentration may be ascribed to NiO precipitation so Ni atoms no longer occupy octahedral sites where Co^{3+} are originally located. This increase might also be due to the ambient annealing during which the catalyst surface is oxidized by atmospheric O_2. Fig. S5 displays the light-off curves of propane oxidation for $NiCo_2O_4$ nano-arrays annealed at different temperatures. High temperature annealing (450 °C and 600 °C) results in worse catalytic activity due to the decreased catalyst structural stability. Here, 100% propane oxidation can be achieved at temperatures lower than 400 °C where all the Ni doped Co_3O_4 nano-array catalysts are thermally stable. Nevertheless, for other hydrocarbon combustion where higher temperature is required (*e.g.*, methane combustion) a balance between enhanced activity and decreased structural stability of the Ni doped Co_3O_4 nano-array catalysts needs to be considered.

5. Conclusion

In summary, Co_3O_4 based nano-array catalysts have been successfully fabricated and exhibit high activity toward propane oxidation at low temperature. Ni doping was discovered to enhance the reaction kinetics and promote the catalytic activity. *In situ* DRIFTS investigations help reveal the catalytic reaction mechanism with further confirmation by oxygen isotope experiments. The thermal stability of Ni doped Co_3O_4 nano-arrays has been studied by Raman scattering coupled with XPS characterization. The major findings from this study can be summarized as follows.

a The doping of Ni into the spinel Co_3O_4 lattice enhances the reaction kinetics and allows low temperature oxidation by promoting the activity of lattice oxygen and creating oxygen defects on the catalyst surface.

b The Ni doping is discovered to favor the formation of thermally less stable carbonates (bidentate and bicarbonate species) on the catalyst surface and thus facilitates CO_2 desorption at lower temperature.

c Surface chlorine on Co_3O_4 nano-arrays has been found to be detrimental to propane oxidation, due to either blocking of the active sites or passivation of the Co—O bonds on the catalyst surface by Cl.

d *In situ* DRIFTS in addition to oxygen isotope experiments reveals the catalytic propane oxidation proceeds *via* the Mars-van Krevelen mechanism where surface lattice oxygen functions as active sites for oxidizing propane.

e Raman scattering, XRD, and XPS analyses confirm the segregation of NiO from the $Ni_xCo_{3-x}O_4$ lattice at high temperature resulting in a decrease of both thermal stability and catalytic activity.

Acknowledgement

Appendix A. Supplementary data

Supplementary data associated with this article can be found, in the online version, at http://dx.doi.org/10.1016/j.apcatb.2015.04.021

References

[1] I. Caplain, F. Cazier, H. Nouali, A. Mercier, J.-C. Déchaux, V. Nollet, R. Joumard, J.-M. André, R. Vidon, Atmos. Environ. 40 (2006) 5954.
[2] R.J. Gordon, H. Mayrsohn, R.M. Ingels, Environ. Sci. Technol. 2 (1968) 1117.
[3] J.J. Schauer, M.J. Kleeman, G.R. Cass, B.R.T. Simoneit, Environ. Sci. Technol. 36 (2002) 1169.
[4] M. Shelef, G.W. Graham, Catal. Rev. 36 (1994) 433.
[5] P. Kočí, M. Kubíček, M. Marek, Ind. Eng. Chem. Res. 43 (2004) 4503.
[6] G.C. Koltsakis, A.M. Stamatelos, Prog. Energy Combust. Sci. 23 (1997) 1.
[7] N. Collins, M. Twigg, Top. Catal. 42–43 (2007) 323.
[8] K. Tikhomirov, O. Kröcher, M. Elsener, A. Wokaun, Appl. Catal. B Environ. 64 (2006) 72.
[9] W. Liu, M. Flytzanistephanopoulos, J. Catal. 153 (1995) 304.
[10] F. Grillo, M.M. Natile, A. Glisenti, Appl. Catal. B Environ. 48 (2004) 267.
[11] Z. Wu, M. Li, S.H. Overbury, J. Catal. 285 (2012) 61.
[12] Z.-R. Tian, W. Tong, J.-Y. Wang, N.-G. Duan, V.V. Krishnan, S.L. Suib, Science 276 (1997) 926.
[13] Q. Fu, F. Yang, X. Bao, Acc. Chem. Res. 46 (2013) 1692.
[14] Z. Zhu, G. Lu, Z. Zhang, Y. Guo, Y. Guo, Y. Wang, ACS Catal. 3 (2013) 1154.
[15] M. Baldi, V.S. Escribano, J.M.G. Amores, F. Milella, G. Busca, Appl. Catal. B Environ. 17 (1998) L175.
[16] T. Seiyama, Catal. Rev. 34 (1992) 281.
[17] H. Arai, T. Yamada, K. Eguchi, T. Seiyama, Appl. Catal. 26 (1986) 265.
[18] C.H. Kim, G. Qi, K. Dahlberg, W. Li, Science 327 (2010) 1624.
[19] G. Saracco, F. Geobaldo, G. Baldi, Appl. Catal. B Environ. 20 (1999) 277.
[20] J.G. McCarty, H. Wise, Catal. Today 8 (1990) 231.
[21] J. Zhu, H. Li, L. Zhong, P. Xiao, X. Xu, X. Yang, Z. Zhao, J. Li, ACS Catal. 4 (2014) 2917.
[22] W. Song, A.S. Poyraz, Y. Meng, Z. Ren, S.-Y. Chen, S.L. Suib, Chem. Mater. 26 (2014) 4629.
[23] X.W. Xie, Y. Li, Z.Q. Liu, M. Haruta, W.J. Shen, Nature 458 (2009) 746.
[24] Y. Guo, Z. Ren, W. Xiao, C. Liu, H. Sharma, H. Gao, A. Mhadeshwar, P.-X. Gao, Nano Energy 2 (2013) 873.
[25] W. Xiao, Y. Guo, Z. Ren, G. Wrobel, Z. Ren, T. Lu, P.-X. Gao, Cryst. Growth Des. 13 (2013) 3657.
[26] Y. Guo, G. Liu, Z. Ren, A. Piyadasa, P.-X. Gao, CrystEngComm 15 (2013) 8345.
[27] Z. Ren, Y. Guo, Z. Zhang, C. Liu, P.-X. Gao, J. Mater. Chem. A 1 (2013) 9897.
[28] Z. Ren, V. Botu, S. Wang, Y. Meng, W. Song, Y. Guo, R. Ramprasad, S.L. Suib, P.-X. Gao, Angew. Chem. Int. Ed. 53 (2014) 7223.
[29] S. Xiong, J.S. Chen, X.W. Lou, H.C. Zeng, Adv. Funct. Mater. 22 (2012) 861.
[30] B. Wang, T. Zhu, H.B. Wu, R. Xu, J.S. Chen, X.W. Lou, Nanoscale 4 (2012) 2145.
[31] Y. Xiao, S. Liu, F. Li, A. Zhang, J. Zhao, S. Fang, D. Jia, Adv. Funct. Mater. 22 (2012) 4051.
[32] Z. Fei, S. He, L. Li, W. Ji, C.-T. Au, Chem. Commun. 48 (2012) 853.
[33] C.-W. Tang, L.-C. Hsu, S.-W. Yu, C.-B. Wang, S.-H. Chien, Vib. Spectrosc. 65 (2013) 110.
[34] J.-Y. Luo, J. Meng, Y.-Q. Zha, L.-H. Guo, J. Phys. Chem. C 112 (2008) 8694.
[35] C. Binet, M. Daturi, J.-C. Lavalley, Catal. Today 50 (1999) 207.
[36] O. Pozdnyakova, D. Teschner, A. Wootsch, J. Kröhnert, B. Steinhauer, H. Sauer, L. Toth, F.C. Jentoft, A. Knop-Gericke, Z. Paál, R. Schlögl, J. Catal. 237 (2006) 17.
[37] C. Doornkamp, V. Ponec, J. Mol. Catal. A: Chem. 162 (2000) 19.
[38] X.-Y. Pang, C. Liu, D.-C. Li, C.-Q. Lv, G.-C. Wang, ChemPhysChem 14 (2013) 204.
[39] R. Grasselli, Top. Catal. 21 (2002) 79.
[40] C. Li, Y. Sakata, T. Arai, K. Domen, K. Maruya, T. Onishi, J. Chem. Soc., Chem. Commun. (1991) 410.
[41] M. Cabo, E. Pellicer, E. Rossinyol, O. Castell, S. Suriñach, M.D. Baró, Cryst. Growth Des. 9 (2009) 4814.
[42] M.N. Iliev, P. Silwal, B. Loukya, R. Datta, D.H. Kim, N.D. Todorov, N. Pachauri, A. Gupta, J. Appl. Phys. (2013) 114.
[43] V.G. Hadjiev, M.N. Iliev, I.V. Vergilov, J. Phys. C: Solid State Phys. 21 (1988) L199.
[44] Z.-Q. Liu, Q.-Z. Xu, J.-Y. Wang, N. Li, S.-H. Guo, Y.-Z. Su, H.-J. Wang, J.-H. Zhang, S. Chen, Int. J. Hydrogen Energy 38 (2013) 6657.